Materials Science & Engineering A 855 (2022) 143889

Contents lists available at ScienceDirect

Materials Science & Engineering A

journal homepage: www.elsevier.com/locate/msea

Size-dependent tensile failure of epitaxial TiN/Cu/TiN sandwich pillar structures: A combined experimentation – Atomistic simulation study

Xiaoman Zhang [a,1], Reza Namakian [a,1], Andrew C. Meng [c], Dorel Moldovan [a,b,*], W.J. Meng [a,**]

[a] Department of Mechanical & Industrial Engineering, Louisiana State University, Baton Rouge, LA, 70803, USA
[b] Center for Computation and Technology, Louisiana State University, Baton Rouge, LA, 70803, USA
[c] Department of Physics and Astronomy, University of Missouri, Columbia, MO, 65211, USA

ARTICLE INFO

Keywords:
Metal/ceramic interfacial failure
Epitaxial growth
Nano-twinned microstructure
Micropillar tension testing
MD simulations
Size dependent failure mode

ABSTRACT

A combined experimentation - molecular dynamics simulation study was conducted to understand tensile failure of TiN/Cu/TiN interfacial regions. Tensile loading was conducted on micro-pillar specimens fabricated from TiN/Cu/TiN thin film sandwich structures. The Cu layer and the TiN layer underneath were grown epitaxially on MgO (001) substrates, with Cu[110]//TiN[001] in the growth direction and Cu<111>//TiN<100> and Cu<112>//TiN<100> within the growth plane. The Cu layer contains numerous nanotwins with the {111} twin plane parallel to the growth direction, with 2–10 nm wide twin bands rotated in-plane by 90° in different yet symmetry-equivalent epitaxial domains. Tensile loading in-situ a scanning electron microscope measured tensile fracture stress ~1.5 GPa and revealed a surprising failure mode transition. At a larger Cu layer thickness, ductile tensile fracture occurred within the Cu layer. At smaller Cu layer thicknesses, apparently brittle fracture occurred close to or at the Cu/TiN interface. The accompanying molecular dynamics simulations illustrate a significant dependence of the failure mode on the aspect ratio of Cu pillars under tensile loading. With pillars of small height-to-diameter ratios, tensile loading leads to a significant hydrostatic tension within, as well as significant plasticity throughout the Cu pillar, in particular near the top and bottom Cu/TiN interfaces. The high degree of dislocation activities close to or at the interface, combined with dislocation pile-up, serves to create nanovoids. The high hydrostatic tension furnishes a driving force for growth of such nanovoids, leading to rapid tensile fracture. The simulation results offer an analogy to experimental observations and mechanistic understanding of tensile failure mechanisms for ceramic/metal/ceramic interfacial regions.

1. Introduction

Mechanical integrity of ceramic/metal interfaces impacts diverse technological applications, including metal/ceramic composites [1], VLSI interconnects [2], and hard coatings [3]. Tests have been devised for evaluating the mechanical integrity of adhesive joints under both shear and tensile loading, such as the single lap joint test, the pull-off test, the three-point-bending test, and the T-peel test [4,5], and protocols have been established for such macroscale tests [6–10], subjected to limitations of low strength of adhesive bonds [11].

Thin ceramic coatings deposited onto metallic substrates offer a prime example of strong ceramic/metal interfaces. Engineering applications, including ceramic coatings for machining tools [12] and mechanical components [13,14], demand mechanically strong interfaces as a prerequisite for deployment. The high interfacial strengths for such coating/substrate systems coupled with the small coating thicknesses, typically less than 10 μm, negate the use of macroscale testing protocols cited above for evaluating such interfaces.

Quantitative measurements of the strength of coating/substrate interfaces and understanding of the key physical elements controlling it are of long-standing interest [15,16]. An adhesion promoting metallic interlayer is often deposited in between the ceramic coating and the substrate, forming a coating/interlayer/substrate sandwich structure. For example, such thin film sandwich structures are now routinely employed in tool coatings [17]. The laser spallation test has been used to measure the tensile strengths of interfaces between thin films/coatings

* Corresponding author. Department of Mechanical & Industrial Engineering, Louisiana State University, Baton Rouge, LA, 70803, USA.
** Corresponding author.
E-mail addresses: dmoldo1@lsu.edu (D. Moldovan), wmeng1@lsu.edu (W.J. Meng).
[1] Authors who have contributed equally to this article.

https://doi.org/10.1016/j.msea.2022.143889
Received 25 July 2022; Received in revised form 24 August 2022; Accepted 25 August 2022
Available online 30 August 2022

and substrates with and without adhesion-promoting interlayers, and can generate quantitative results on films with sub-micron thicknesses. However, the shock wave generation by nanosecond pulsed laser impact onto the substrate leads to very high strain rates, $\sim 10^8$/sec [18]. Experimental testing that can reliably induce tensile failures of strong interfaces at low strain rates has not appeared in the literature until very recently.

Recent activities in small scale mechanical measurements have been enabled by advances in focused ion beam (FIB) nano/micro scale machining [19] and instrumented nano/micro scale mechanical actuation, enabling micron scale mechanical testing in-situ scanning electron microscopes (SEMs) [20]. In a previous paper, we reported results of tensile loading in-situ an SEM of micro-pillar specimens fabricated from CrN/Cu/CrN nanocrystalline thin film sandwich structures vapor deposited onto Si substrates, with the tension direction perpendicular to the CrN/Cu interfaces. Tensile interfacial failure was observed to occur close to one Cu/CrN interface. The tensile fracture stress was observed to increase monotonically with decreasing Cu interlayer thickness, reaching ~2 GPa at a Cu thickness of ~200 nm [21]. While these preliminary results show the promise of the micron scale mechanical testing protocol, the structural complexities of the nanocrystalline CrN/Cu/CrN sandwich specimens complicate mechanistic interpretation of the experimental observations.

To alleviate such structural complexities and the difficulties they bring to interpretation of mechanical testing data, mechanical testing of metal/ceramic interfaces with better-defined structures is desirable. The present work on TiN/Cu/TiN thin film sandwich structures aims to fulfil this task. TiN is a prototypical refractory ceramic [22]. Epitaxial growth of TiN thin films has been shown on various substrates, including MgO [23], Si [24], and Al_2O_3 [25]. In a previous study, the present authors have shown that Cu can be grown epitaxially onto TiN(001) templates in the usual "cube-on-cube" orientation as well as a new orientation in which Cu[110]//TiN[001] in the growth direction, and Cu<111>//TiN<100> and Cu<112>//TiN<100> within the growth plane. The [110] oriented epitaxial Cu layer contains 90°-rotated in-plane domains with numerous Cu{111} twin planes with nm spacings and parallel to the growth direction [26]. Accompanying molecular dynamics/Monte Carlo (MD/MC) simulations revealed that this new Cu/TiN orientation results from a martensitic transformation from an initial BCC Cu layer to a nano-twinned FCC Cu layer [27]. The Cu [110]//TiN[001] structure offers a well-defined epitaxial interface, and an opportunity to study the influence of the presence of numerous Cu nanotwins, with twin plane parallel to the tensile loading direction, on the mechanical response.

Adhesion of solid/solid interfaces and their strengths have also been a subject of long-standing interest for materials theories and simulations. Density functional theory (DFT) has been used to calculate work of adhesion of different metal/ceramic interfaces, e.g., Al/MgO and Ag/MgO interfaces [28], interfaces between Al and various carbides, nitrides, and oxides [29], and NiAl/Al_2O_3 interface [30]. Adhesive properties of Mo/$MoSi_2$ heterophase interfaces have been calculated by DFT, including the effects of interfacial impurities on adhesion. Total energy was calculated as a function of Mo–$MoSi_2$ interfacial separations, and the calculated peak interfacial strengths in all cases exceeded 20 GPa [31]. DFT calculated peak interfacial strengths, representing ideal tensile interfacial separation, are typically high, e.g., ~10 GPa for Al/MgO and Ag/MgO [32], significantly exceeding experimentally measured values [20]. The discrepancy between DFT calculated ideal interfacial tensile strength and experimentally measured tensile fracture stress suggest that additional physics needs to be considered to better understand the mechanical response of metal/ceramic interfaces.

In this paper, we describe the outcomes of a combined experimentation and molecular dynamics (MD) simulation study. Trilayer TiN/Cu/TiN sandwich structures, with the Cu layer in the Cu[110]//TiN[001] orientation relationship and containing numerous nanotwins, were prepared with ultra-high-vacuum (UHV) vapor phase deposition. Micron sized TiN/Cu/TiN cylindrical pillar specimens with TiN/Cu/TiN interfaces perpendicular to the pillar axis were fabricated with scripted FIB milling. Mechanical responses of TiN/Cu/TiN interfacial regions under tensile loading, up to and including tensile fracture, were examined with an instrumented nano/micro actuator in-situ an SEM. The experiments observed a surprising failure mode switch as the Cu layer thickness decreases. As the ratio of the Cu layer thickness, H, to micro-pillar diameter, D, decreases, the observed tensile failure modes changes from apparently ductile separation within the Cu layer to apparently brittle fracture close to or at the Cu/TiN interface. The accompanying MD simulations reveal atomistic details of this size-dependent mechanical response and offer mechanistic interpretations of the experimental findings.

2. Methodology

2.1. Experimental procedures

Two-side polished MgO(001) wafers (99.99%), with dimensions of $10 \times 10 \times 0.5$ mm^3, were cleaned with successive rinses in ultrasonic baths of acetone and ethanol, and blown dry with dry N_2. Cleaned MgO substrates were mounted with one side covered in a stainless-steel holder and loaded into a high vacuum chamber with base pressure $<1 \times 10^{-8}$ Torr. The exposed side of the MgO substrate was then etched in an Ar (99.999%+) inductively coupled plasma (ICP) for ~3 min at a −50 V bias, followed by elemental Si (99.95%) deposition from a 7.5 cm diameter Si magnetron sputter source in Ar without intentional heating. The thickness of the deposited Si layer was ~1 μm.

The one-side Si-deposited MgO(001) wafer was unloaded from the high vacuum system, mounted onto another Mo holder, and inserted into a load-lock chamber for transport into an UHV dc magnetron sputter deposition chamber with a base pressure $<5 \times 10^{-10}$ Torr. The deposition chamber houses two 7.5 cm diameter Ti (99.95%) magnetron sputter sources, one 7.5 cm diameter Cu (99.99%) magnetron sputter source, and a high temperature substrate stage with radiation heating from a SiC heating element. The Si-deposited side of the MgO wafer faced the heating elements and the not-deposited side of the MgO wafer faced the incoming vapor flux through a hole in the Mo holder. The actual substrate temperature was determined by measuring the temperature of a pristine Si wafer mounted onto the same Mo holder through direct optical access infrared pyrometry, with the Si wafer emissivity set at 0.68. Substrate temperature monitoring was accomplished by a separate thermocouple placed in close proximity to the Mo holder. A substrate temperature calibration curve was established by conducting multiple measurements of the Si wafer temperature with the infrared pyrometer, while conducting simultaneous thermocouple temperature readings. During growth onto backside-Si-deposited MgO (001) wafers, the deposition temperature was determined from the thermocouple reading, cross referenced to the temperature calibration curve.

The MgO(001) wafers were heated in the UHV deposition chamber at ~850 °C for 20 min. Sputter deposition of TiN commenced immediately after at the same temperature, with two Ti magnetron sources operated in a constant current mode at 1.65 A in an Ar/N_2 (99.999%+/99.999%) mixture and at a total pressure of ~4.5 mTorr. A substrate bias of −40 V was applied. The N_2 input flow rate was adjusted to be close to the point of stoichiometric deposition. The typical deposition rate for TiN is ~2.6 Å/s. The thickness of this TiN layer was ~4 μm. After TiN deposition on MgO(001), the substrate temperature was decreased and equilibrated at ~95 °C. Sputter deposition of Cu commenced on the TiN layer in ~4 mTorr of pure Ar after temperature equilibration. The Cu magnetron source operated in a constant current mode at 1.35 A with no substrate bias voltage applied. The typical deposition rate for Cu is ~3 Å/s, and the duration of Cu deposition was controlled to control the thickness of the deposited Cu layer. After Cu deposition, the substrate temperature was increased and equilibrated at 650 °C. Deposition of another layer of

TiN on top of the Cu layer commenced after temperature equilibration, at the same Ti gun currents, Ar/N_2 input flow rates, and total pressure, with a −50 V substrate bias voltage applied. The thickness of this top TiN layer was again ~4 μm. The entire deposition sequence led to the formation of TiN/Cu/TiN thin film sandwich structures on MgO(001) substrate, with the Cu layer thickness H ranging from >50 nm to < 1000 nm. Additional details on the vapor deposition procedure have been described elsewhere [25,26].

The TiN/Cu/TiN/MgO(001) thin film was allowed to cool to close to room temperature after deposition before transferred out of the UHV deposition system, mounted in another stainless steel holder with the top TiN film side exposed and inserted into a load-lock chamber for transport back into the first magnetron sputter deposition chamber with a base pressure $<1 \times 10^{-8}$ Torr. The exposed TiN side was then etched in an Ar ICP for ~3 min at a −50 V bias, followed by elemental Cr (99.95%) deposition in pure Ar from two 7.5 cm diameter Cr magnetron sputter sources without intentional heating. The thickness of this deposited Cr layer was ~1 μm. Its purpose is to facilitate fabrication of micro-pillar tensile specimens, as described below.

The structure and morphology of Cr/TiN/Cu/TiN/MgO(001) specimens with varying Cu layer thicknesses were characterized by X-ray diffraction (XRD), SEM, and transmission electron microscopy (TEM). X-ray θ/2θ scan, ω rocking curve scan, and asymmetric φ scan were collected on a PANalytical Empyrean system. Scanning imaging with electron- or ion-induced secondary electrons (SE/ISE) and Ga^+ FIB milling were carried out on an FEI Quanta3D Dual-Beam FEG instrument, which houses an EDAX X-ray energy dispersive spectroscopy (EDS) system and an OmniProbe system for site-selective specimen lift-out. A JEOL JEM-2011 microscope and a JEOL JEM-F200 microscope, both operated at 200 kV, were used for TEM examinations.

"Mushroom-shaped" cylindrical micro-pillar specimens with TiN/Cu/TiN interfaces perpendicular to the pillar axes were fabricated from Cr/TiN/Cu/TiN/MgO(001) thin films by Ga^+ FIB milling. Sequential sideways scripted FIB milling yielded the final micro-pillar structure with a tapered "mushroom cap" top portion consisting of only the TiN top layers, a tapered "mushroom stem" bottom portion consisting of only the TiN bottom layer next to the MgO(001) substrate, and a tensile gauge portion including the TiN/Cu/TiN interfaces. The tensile gauge section has the smallest diameter, D = 2–3 μm. Further details on the scripted FIB milling process have been reported previously [20].

In-situ tensile loading of mushroom shaped Cr/TiN/Cu/TiN micro-pillars was conducted on a NanoMechanics Inc. NanoFlip® instrumented micro/nano mechanical testing device, placed within and coupled to the FEI Quanta3D FIB instrument. A custom fabricated diamond hook with an "inverse V″ shaped slot was used to engage the top portion of the mushroom shaped micro-pillar specimen and apply the tensile load. Repeat axial tension tests were carried out on multiple micro-pillar specimens. The diamond hook was actuated in a displacement-controlled mode with a target displacement rate of 5 nm/s. For Cu layer thicknesses within the range of 50 nm–500 nm, the nominal strain rates thus range from 10^{-2}/sec to 10^{-1}/sec. The tensile load, P, was continuous recorded during displacement-controlled loading until specimen fracture occurred.

2.2. Simulation methodology

The MD simulations were performed by using the Large-scale Atomic/Molecular Massively Parallel Simulator (LAMMPS) [33] package. To ensure accurate description of dislocation-dislocation and dislocation-twin boundary (TB) interactions in Cu, the embedded atom method (EAM) potential developed by Mishin et al. [34] was used. This potential was utilized recently by Ko et al. [35] in atomistic simulation studies of interactions between dislocations and TBs. The Atomsk software package [36] was used to assemble the simulation nanocrystalline pillar systems and tailor their grain and TBs network structure. The various post-processing analyses, including visualization of atomic structures as well as detailed crystal structure and defect analysis as revealed via the interval common neighbor analysis (ICNA) methodology [37], were performed in OVITO [38].

Tensile testing experiments were conducted on FIB milled TiN/Cu/TiN cylindrical micro-pillars having tensile gauge sections with diameter D in the 2–3 μm range and thickness of the Cu layer H ranging from 70 nm to 400 nm. Given that MD simulation studies of Cu pillar systems of similar size would be prohibitively expensive, we focused our studies on two cylindrical nano-pillar geometries, with diameters of 93 nm and 45 nm respectively. To mimic the experimental conditions, we investigated the effect of the Cu pillar height-to-diameter ratio (H/D) on the deformation process by choosing H/D values similar to those for pillars used in the experiments. Two simulation pillar systems were considered: the simulated pillar with $H/D < 1$ will be referred to as disk-shaped and the one with $H/D > 1$ will be referred to as rod-shaped. As depicted in Fig. 1, the Cu pillar system consists of a cylindrical gauge region of diameter D and height H, sandwiched between two 4 nm thick rigid Cu slabs. The two slabs can be viewed as infinite in the X and Y directions under the periodic boundary conditions considered along those directions. In both the cylinder and the slab portions, the simulation system consists of four columnar Cu grains with their [110] directions oriented in parallel with the Z direction and internal nano-twins within each grain. The nano-twinned grains making up the Cu pillar system were created by inserting into each grain a regular set of parallel TBs that are 5 nm apart from each other, with the twin planes oriented parallel to the Z direction. To mimic the microstructure of Cu pillars used in experiments, the TBs in each grain were rotated by 90° with respect to the orientation of TB network in the neighboring grains. Fig. 1(a) shows the Cu nano-twinned disk-shaped pillar (NTDP) used in the MD simulations, with $H = 15$ nm, $D = 93$ nm, and $H/D = 0.161$. The simulation box for the NTDP system has dimensions of $L_X = 100$ nm × $L_Y = 100$ nm × $L_Z = 23$ nm, and contains 14,780,252 Cu atoms. The nanotwins can be clearly seen by observing that the atoms located on TBs have HCP coordination (colored in red). Fig. 1(b) shows the Cu nano-twinned rod-shaped pillar (NTRP) used in the MD simulations, with $H = 66$ nm, $D = 45$ nm, and $H/D = 1.47$. The simulation box for the NTRP system has dimensions of $L_X = 50.3$ nm × $L_Y = 50.3$ nm × $L_Z = 74.5$ nm, and contains 9,985,342 Cu atoms. It should be noted that the number of Cu atoms contained in the cylinder portion of both simulated systems is about the same (8,363,000 atoms).

The in-plane dimensions (along X and Y directions) of the slabs capping the cylindrical nanopillars were chosen such that, under periodic boundary conditions considered in the MD simulations, the distance between one pillar and its neighboring periodic images was ~5.5 nm. The components of the atomic stress tensor were computed by following [39,40]. Voronoi tessellation was performed at the location of each atom and used for the evaluation of the local atomic volume. The volume of the cylindrical region at a given time was estimated by summing up all atomic volumes and used in the calculation of the stress components in the cylindrical portion of the nanopillar. In addition, given the high strain rate used in MD simulations [34], the temperature in the nanopillars was controlled by thermostatting only two, 2 nm thick, buffer zones located respectively above and below the cylindrical region of the simulation system. The standard velocity-Verlet integrator was used, and the timestep was adjusted at each iteration such that no atom in the system was displaced a distance greater than 0.02 Å. This approach was used to obtain a balance between the computational efficiency and accuracy.

The as-prepared simulation systems were first subjected to energy minimization via the damped dynamics method of fast inertial relaxation engine (FIRE) [41] with the stopping tolerance values of 10^{-3} meV and 10^{-3} meV/Å for energies and forces, respectively. Then, the Bussi-Donadio-Parrinello (BDP) thermostat [42] with a temperature damping parameter of 10 fs was applied only to the atoms in the buffer zones. Subsequently, a time integration consisting of 650,000 time steps of the simulation system in the microcanonical ensemble (NVE) was

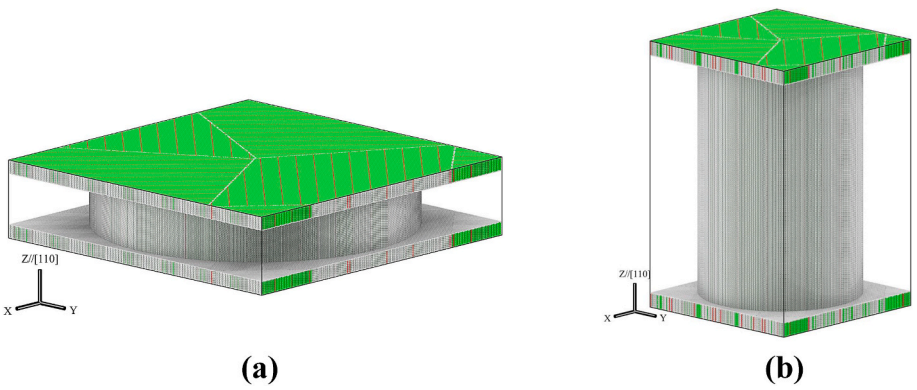

Fig. 1. (a) Cu nano-twinned disk-shaped pillar (NTDP) with $H = 15$ nm, $D = 93$ nm, $H/D = 0.1613$, and two semi-infinite Cu slabs at its top and bottom, each with a thickness of 4 nm; **(b)** Cu nano-twinned rod-shaped pillar (NTRP) with $H = 66$ nm, $D = 45$ nm, $H/D = 1.47$. Atoms were colored according to ICNA analysis: blue = BCC, red = HCP, green = FCC, and light-gray = unidentified crystal structure. (For interpretation of the references to color in this figure legend, the reader is referred to the Web version of this article.)

used to thermally equilibrate the pillar system at 300 K.

After the energy minimization and thermal equilibration stage, the outmost 2 nm thick slab regions along the Z direction, at the very top and the very bottom in Fig. 1(a) and (b), were singled out by setting the force components in all directions and on all atoms to zero thus rendering these regions to behave like infinitely rigid non-deformable walls. This setup is used as a substitute to mimic the experimental situation where the TiN layers with substantially higher mechanical rigidity are in contact with the nano-twinned Cu layer; a reasonable approximation considering that the elastic constants of TiN are much larger than those for Cu (e.g., the Young's moduli of TiN and Cu are $\geq$400 GPa and ~120 GPa, respectively). These rigid walls at the top and the bottom of the Cu nanopillars were subsequently set in motion, in opposite directions along the Z-axis, with a constant velocity such that a steady tensile strain of the Cu pillar gauge region was induced at a strain rate of approximately 10^8 1/s. These very high strain rates, which are over nine orders of magnitude higher than those employed in the experiments, are typical in MD simulations.

As will be demonstrated in this paper, the mechanical response of TiN/Cu/TiN thin film sandwich structures under tensile loading is dominated by dislocation activities within the Cu layer and at/close to the TiN/Cu interface. The TiN layers present an impenetrable barrier for dislocations, such that dislocations coming to the TiN/Cu interface pile up there and lead to formation of excess vacancies and incipient voids. In order to accurately capture the dominant physical processes through MD simulations, it is paramount that the MD potential adopted accurately describes dislocation-dislocation and dislocation-TB interactions in Cu. This provides the main motivation for adopting in the present study the EAM potential for Cu by Mishin et al. [34]. Although one set of interatomic potentials for the ternary Cu–Ti–N system has appeared recently in the literature [43], its efficacy for modeling dislocation-dislocation and dislocation-TB interactions in Cu has not been demonstrated. The

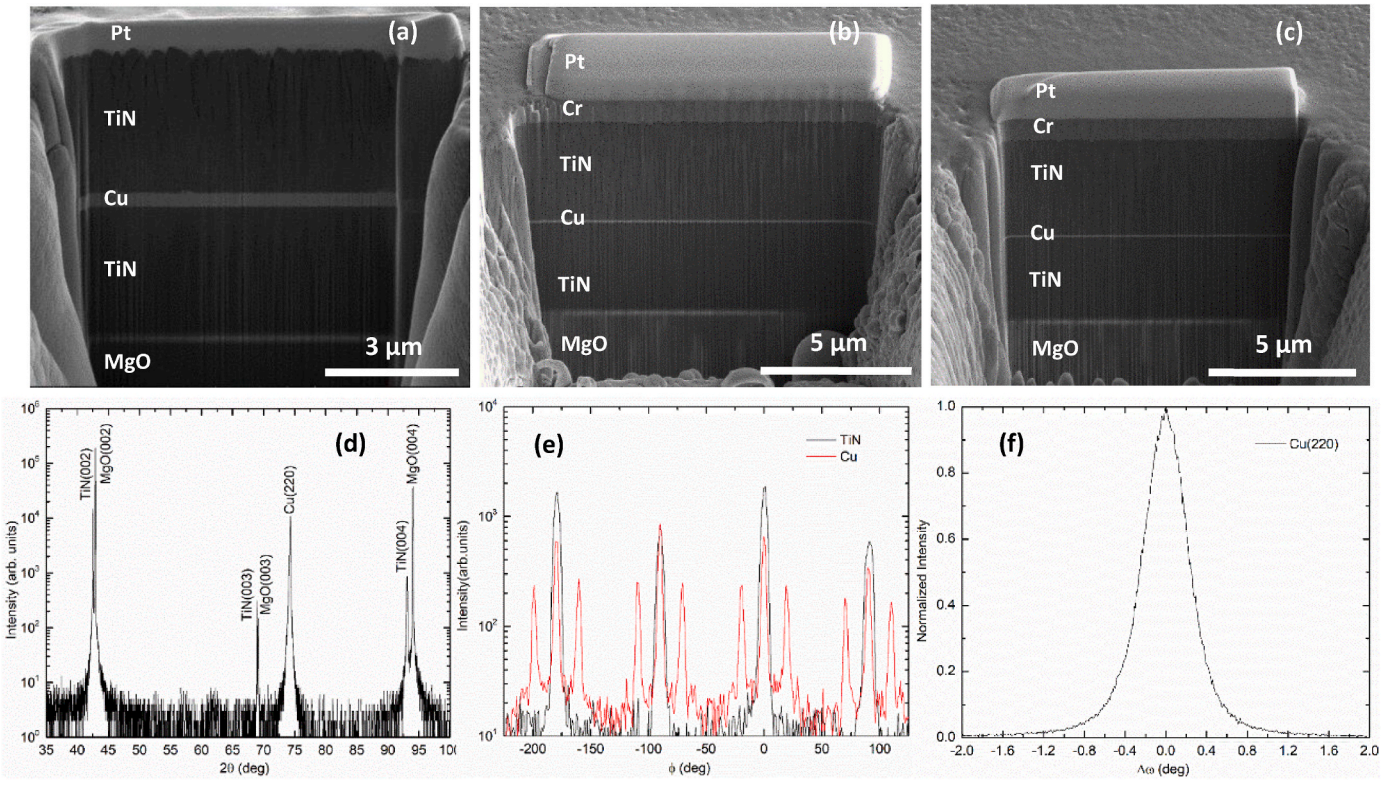

Fig. 2. (a/b/c) Cross-sectional SE images (taken at a 52° tilt) of TiN/Cu/TiN/MgO(001) specimens with a Cu layer thickness of (a) 400 nm; (b) 110 nm; (c) 70 nm. A Cr layer was deposited onto the TiN top layer at room temperature to facilitate subsequent micro tensile specimen fabrication. Pt was deposited onto the specimen top surface prior to Ga + FIB milling to protect the specimen surface from ion beam damage. **(d/e/f)** XRD results from one Cu/TiN/MgO(001) bilayer specimen with a Cu layer thickness of 380 nm: (d) θ/2θ scan; (e) 360° φ scans on TiN(204) and Cu(402) reflections; (f) ω rocking curve scan on Cu(220) reflection.

scheme of replacing the TiN/Cu interface by an infinitely rigid non-deformable wall, described in the preceding paragraph, is believed to be a good compromise without sacrificing the critical physics elements in the present problem. This type of boundary condition is indeed similar to that used in one of our previous studies using crystal plasticity finite element analysis (CPFEA) simulations [21], in which a Cu interlayer was capped between two mechanically rigid loading plates to mimic the mechanical behavior of a ceramic/metal/ceramic sandwich structure.

3. Results

3.1. Experimental observations

Typical morphology of TiN/Cu/TiN thin film specimens is shown in Fig. 2(a/b/c). The cross-sectional SE images show that flat layers of Cu are sandwiched between two ~4 μm thick TiN layers. The same morphology is observed as the Cu layer thickness H (height of Cu nanopillars in the MD simulations) decreases from 400 nm to 110 nm and 70 nm: the entire sandwich specimen is dense and without voids.

The XRD results shown in Fig. 2(d/e/f), obtained from a Cu/TiN/MgO(001) bilayer specimen with a Cu layer thickness of 380 nm, illustrate typical film structure and orientation relationship. The θ/2θ scan, Fig. 2(d), shows (002) and (004) reflections of MgO and TiN, indicating complete TiN texture with TiN[001]//MgO[001]. The only Cu reflection observed is (220), showing complete Cu texture with Cu [110]//TiN[001]. The 360° φ scan, Fig. 2(e), shows four TiN (204) reflections, 90° spaced and aligned with four MgO (204) reflections (not shown for clarity). The TiN layer grown on MgO(001) is therefore aligned with the MgO substrate epitaxially in the "cube on cube" orientation, with TiN[001]//MgO[001] in the growth direction and TiN<100>//MgO<100> in the growth plane. Also observed are four groups of triplet Cu(402) reflections, 90° spaced with the middle reflection aligned with the TiN(204) reflection. The spacing between the

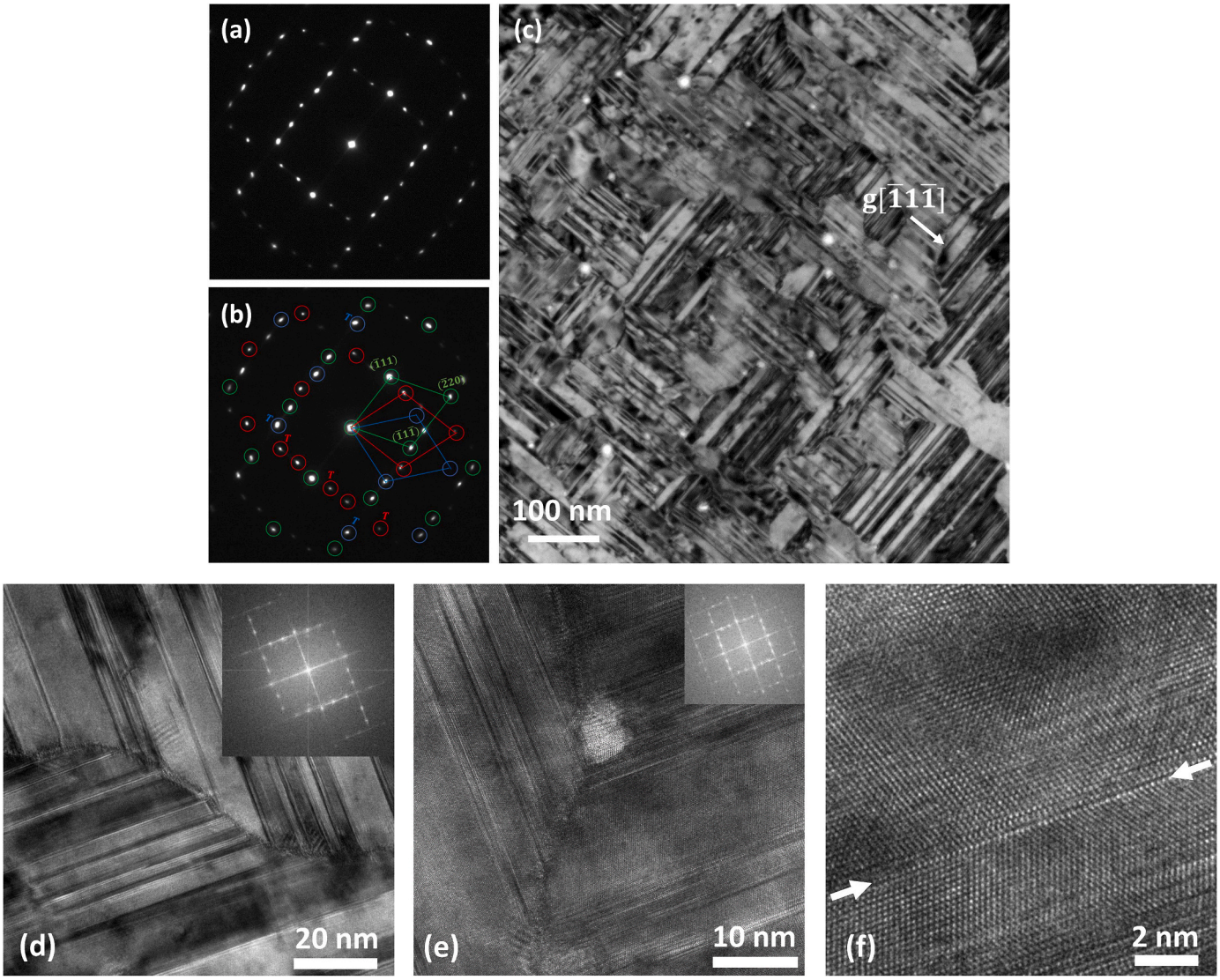

Fig. 3. Plan-view TEM characterization of the Cu layer of one Cu/TiN bilayer specimen with Cu(110)//TiN(001)//MgO(001): **(a)** a plan-view SAD pattern from the Cu top layer with the electron beam parallel to the growth direction; **(b)** the same SAD pattern together with indexing, consisting of a superposition of three Cu [110] zone axis diffraction patterns in red, green, and blue circles. For clarity, (hkl) designations are only shown for the green pattern. The symbol T denotes {111} twinning spots; **(c)** a BF image of the Cu top layer. The arrow denotes the $[\bar{1}1\bar{1}]$ reciprocal lattice vector of the red pattern shown in (b); **(d/e)** phase contrast images of the Cu top layer showing Cu twin bands intersecting at 90°. The insets show respectively the corresponding FFTs of the images; **(f)** a phase contrast image showing one coherent Cu twin boundary, highlighted by the pair of white arrows. (For interpretation of the references to color in this figure legend, the reader is referred to the Web version of this article.)

three Cu(402) peaks in one triplet is ~19.6°. As shown previously, the Cu/TiN orientation relationship that results in the θ/2θ and φ scan patterns shown in Fig. 2(d/e) is Cu[110]//TiN[001] in the growth direction, Cu<111>//TiN<100> and Cu<112>//TiN<100> in the growth plane [25]. Four symmetry equivalent orientation variants exist, all with Cu[110]//TiN[001] in the growth direction. The in-plane orientation relationships are: Cu $[\bar{1}12]$//TiN[100], and Cu $[\bar{1}1\bar{1}]$//TiN $[0\bar{1}0]$ (variant A); Cu$[\bar{1}12]$//TiN [010] and Cu$[\bar{1}1\bar{1}]$//TiN[100] (variant B); Cu $[\bar{1}1\bar{2}]$//TiN $[\bar{1}00]$ and Cu $[\bar{1}11]$//TiN$[0\bar{1}0]$ (variant C); Cu$[\bar{1}1\bar{2}]$//TiN $[0\bar{1}0]$ and Cu $[\bar{1}11]$//TiN[100] (variant D). Variants A and B are rotated 90° in-plane with respect to each other. Variants A and C are twin-related, with the {111} twin plane perpendicular to TiN[010]. Variants B and D are twin-related, with the {111} twin plane perpendicular to TiN[100] [25,26]. The degree of growth direction crystallographic alignment for Cu is illustrated by the ω rocking curve scan on the Cu(220) reflection, Fig. 2(f). The full width at half maximum (FWHM) is ~0.8°. Data shown in Fig. 2(d/e/f) indicate that the Cu/TiN bilayer is fully epitaxial on MgO(001).

Corresponding plan-view TEM results are shown in Fig. 3, obtained from a Cu/TiN/Mg(001) bilayer with a Cu layer thickness of 380 nm. The plan-view TEM specimen was prepared by OmniProbe lift-out of a Cu/TiN/MgO(001) specimen segment in the cross section orientation, followed by Ga^+ ion beam thinning from the TiN/MgO side until all TiN/MgO is removed, leaving only the Cu top layer. A final polishing using 100 eV Ar^+ ion polishing was used to thin the Cu layer to electron transparency. Fig. 3(a) shows a selected area electron diffraction (SAED) pattern obtained from the Cu layer, with the electron beam placed approximately parallel to the growth direction. The same SAED pattern is shown again in Fig. 3(b), together with the indexing. The SAED pattern consists of a superimposition of three Cu[110] zone axis diffraction patterns, in-plane rotated with respect to each other by ~ ±19.5°, consistent with the XRD results shown in Fig. 2(e). In addition to Cu[110] zone axis diffraction spots, twinning spots with respect to in-plane <111> directions are observed. Fig. 3(c) shows the corresponding bright field (BF) image. Irregular shaped domains nestled together to form one continuous Cu layer. Within each domain, dense nanoscale twin planes are present, perpendicular to the in-plane <111> direction with twin plane spacings of 2–10 nm. The in-plane <111> nanotwins exist in two mutually perpendicular directions, consistent with XRD data presented in Fig. 2. Fig. 3(d) and (e) show high-resolution phase contrast images of the Cu top layer. Cu twin bands intersecting at 90° are clearly shown. Insets in Fig. 3(d) and (e) show respectively the Fast Fourier Transforms (FFTs) associated with the images. The FFTs are consistent with the SAED pattern shown in Fig. 3(a). Fig. 3(f) shows the phase contrast image of a typical coherent Cu twin boundary, indicating that the Cu {111} twin plane is parallel to the Cu[110]//TiN[001] growth direction. The structure of the epitaxial Cu film, with the presence of dense Cu nanotwins with {111} twin planes parallel to the growth direction, is unique, as twinning in vapor deposited Cu is most often observed with {111} twin planes perpendicular to the growth direction [44]. In addition, the epitaxial growth of Cu, as documented in Figs. 2 and 3, offers well-defined epitaxial Cu/TiN interface.

The XRD results shown in Fig. 4, obtained from a TiN/Cu/TiN/Mg (001) trilayer with a Cu layer thickness of 400 nm, illustrate typical film structure and orientation relationship of TiN/Cu/TiN sandwich specimens. The θ/2θ scan, Fig. 4(a), shows again (002) and (004) reflections of MgO and TiN and (220) reflection of Cu, indicating the persistence of the Cu[110]//TiN[001]//MgO[001] texture in the growth direction. The Cu(220) reflection intensity is significantly diminished as compared to that shown in Fig. 2(d) due to the attenuation from the ~4 μm TiN top layer. The 360° φ scan, Fig. 4(b), shows again four TiN(204) reflections 90° spaced and aligned with four MgO(204) reflections (not shown for clarity). Four groups of triplet Cu(402) reflections are again observed to be 90° spaced with the middle reflection aligned with the TiN(204) reflection, with the spacing between the three Cu(402) peaks in one triplet being ~19.6°. The Cu (402) triplet intensity is again diminished while the TiN(204) intensity is significantly higher due to the presence of the ~4 μm TiN top layer. The ω rocking curve scan on the Cu(220) reflection is shown in Fig. 4(c), the FWHM of which is ~0.6°, showing the degree of growth direction crystallographic alignment of the Cu layer. Additional TiN(111)/(222) and Cu(002) reflections are observed in the θ/2θ scan shown in Fig. 4(a). The presence of TiN(111)/(222) reflections in the θ/2θ scan from the trilayer specimen and their absence from the bilayer specimen indicates that the top TiN layer is polycrystalline with a mixture of grains with [111] or [001] parallel to the growth direction. The intensity of the Cu(002) reflection is about one order of magnitude lower than the Cu(220) reflection. Coupled with the φ scan data shown in Fig. 4(b), the diffraction data indicate that the Cu layer in the TiN/Cu/TiN trilayer sandwich specimens adopts the same epitaxial orientation relationship as detailed for the Cu/TiN bilayer specimen, albeit with a minor non-epitaxial component of [001] oriented Cu.

Fig. 5(a) shows an ISE image of a typical TiN/Cu/TiN/MgO(001) micro-pillar tensile specimen with a Cu layer thickness of 400 nm. The two ~4 μm thick TiN layers allows the micro-pillar specimen to be fabricated entirely within the TiN/Cu/TiN sandwich structure. Sideways scripted Ga + ion milling was executed in several steps to create micro-pillars with tapered gauge sections in the middle, Fig. 5(a), so that the applied stress is the highest at the TiN/Cu/TiN section once the "inverse-V" diamond hook, a part of the actuator that applies the tensile load, engages the mushroom shaped top portion of the micro-pillar specimen, Fig. 5(b). Fig. 5(c) shows values of tensile failure stress σ_f, obtained by dividing the measured tensile failure load, P_f, by the cross-sectional area of the TiN/Cu/TiN gauge section, $4P_f/\pi D^2$, plotted versus the thickness of the Cu layer, H. Multiple data points at the same H value denote

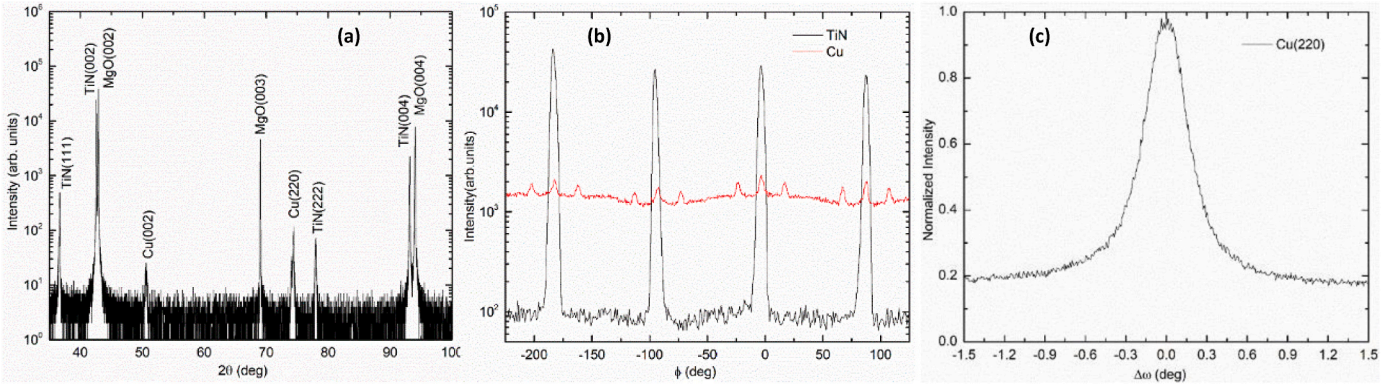

Fig. 4. XRD results from one TiN/Cu/TiN sandwich specimen with a Cu layer thickness of 400 nm: **(a)** θ/2θ scan; **(b)** 360° φ scans on TiN(204) and Cu(402) reflections; **(c)** ω rocking curve scan on Cu(220) reflection.

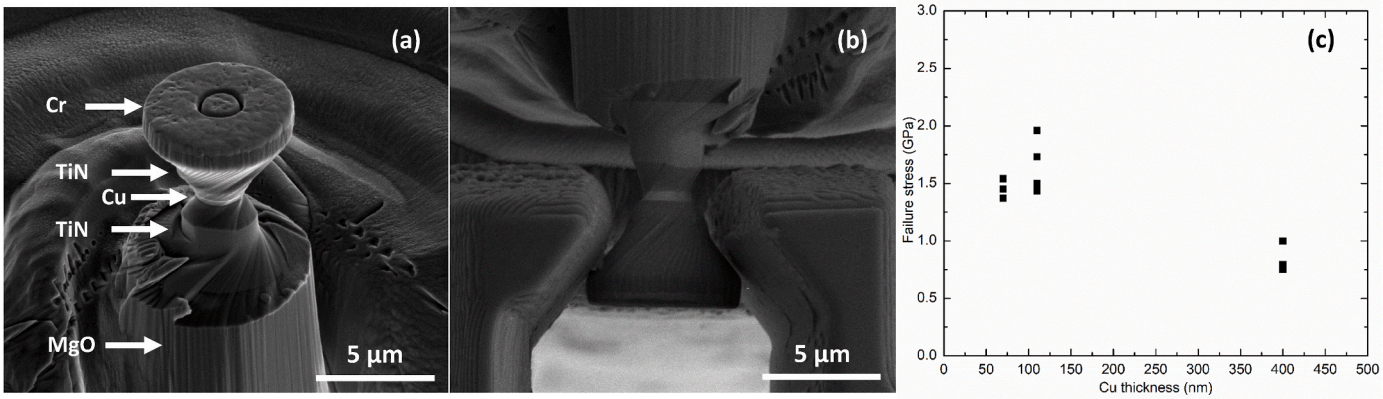

Fig. 5. Micro-pillar tension testing: **(a)** an ISE image of a typical TiN/Cu/TiN sandwich micro-pillar tensile specimen with a Cu layer thickness of 400 nm; **(b)** an SE image of the same pillar engaged by a "inverse V" shaped diamond hook prior to actual tensile loading; **(c)** values of tensile failure stress plotted vs. the Cu layer thickness H.

measurements on separate pillar specimens. Data scatter illustrates typical measurement repeatability. σ_f is ~0.9 GPa at $H = 400$ nm, and increases to ~1.5 GPa as H decreases to 110 nm. No further increase in σ_f value was observed as H decreases further from 110 nm to 70 nm.

Fig. 6(a) shows load–displacement data, P–d curves, measured from three separate TiN/Cu/TiN sandwich pillar specimens with Cu layer thickness $H = 400$ nm. In all cases, P increases with increasing d initially and reaches a load plateau, which persists for ~40 nm of displacement, before tensile fracture occurs. Fig. 6(b/c) shows respectively the bottom and top portions of the same pillar specimen after tensile fracture occurred. It is evident that the tensile separation occurred in the middle of the Cu layer: the Cu/TiN interface associated with the bottom pillar portion (Fig. 6(b)) and the TiN/Cu interface associated with the top pillar portion (Fig. 6(c)) are both intact. It is also evident that the Cu layer necked down significantly: the diameter at the final fracture point associated with the bottom pillar portion is ~0.4 μm while the original pillar diameter is ~2 μm, a diameter reduction of ~80%. In addition, one single dimple is evident on the fracture surface associated with the bottom pillar portion (Fig. 6(b)) and a corresponding dimple is evident on the fracture surface associated with the top pillar portion (Fig. 6(c)), suggesting formation of a single void during the last stage of tensile separation. Fig. 6(d/e) show respectively the bottom and top portions of another TiN/Cu/TiN pillar specimen after tensile fracture occurred. Again, The Cu/TiN and TiN/Cu interfaces associated with the bottom and top pillar portions remained intact despite the tensile loading, and the tensile separation occurred in the middle of the Cu layer. The deformation caused the Cu layer to neck down to a single ridge, with corresponding ridge features seen on both the bottom and top portion of the separated pillar specimen. The findings shown in Fig. 6 illustrate the essential observation that tensile fracture of TiN/Cu/TiN sandwich pillar specimens with $H = 400$ nm occurred through extensive plastic deformation within the Cu layer, without inducing failure at the Cu/TiN interfaces.

Fig. 7(a/b) show P–d curves measured from TiN/Cu/TiN sandwich pillar specimens with H of 110 nm and 70 nm, respectively. Contrary to the data shown in Fig. 6 with $H = 400$ nm, measured tensile load increases with increasing displacement until fracture occurs without a load plateau appearing, for both $H = 110$ nm and 70 nm. Fig. 7(c/d) show respectively the bottom and top portions of the same pillar specimen, with $H = 110$ nm, after tensile fracture occurred. In this case, tensile fracture is seen to have occurred close to the top TiN/Cu interface. The bulk of the Cu layer appears relatively undeformed, with little sign of diameter decrease from the original value of ~2.5 μm. Remnants of Cu appear only on the rim of the separated top pillar portion. Fig. 7(e/f) show the corresponding Cu K EDS maps of the bottom and top portions of the same pillar. Consistently, fracture surface of the bottom portion shows uniform Cu signal while Cu intensity is only perceptible around the rim of the fractured pillar top portion. Similar fracture morphology

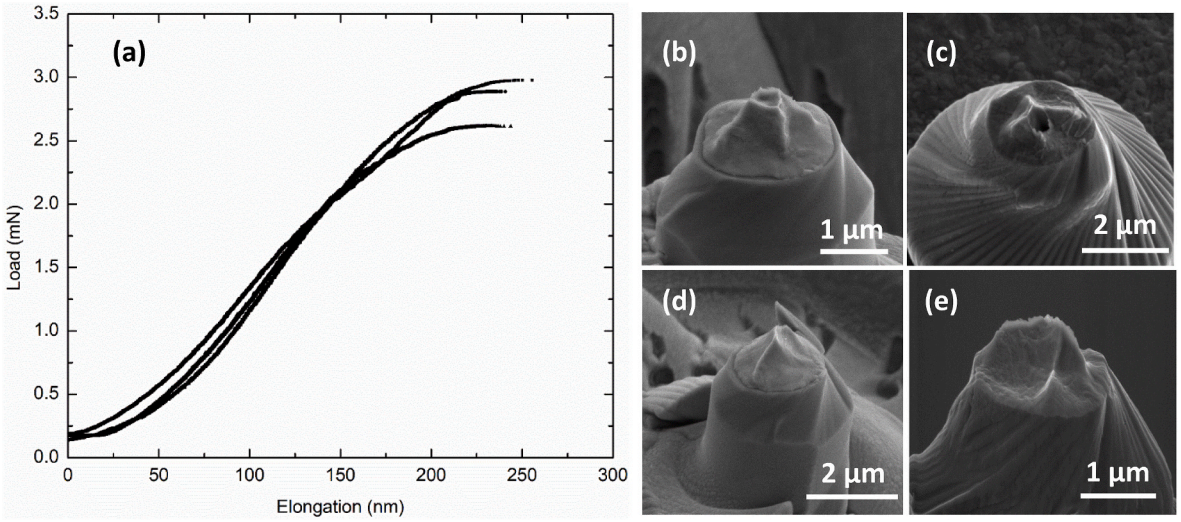

Fig. 6. Tension testing results of TiN/Cu/TiN sandwich micro-pillar specimens with the Cu layer thickness $H = 400$ nm: **(a)** load-elongation curves; **(b/c)** SE images of the bottom and top portions of the same pillar after tensile separation; **(d/e)** SE images of the bottom and top portions of another pillar after tensile separation.

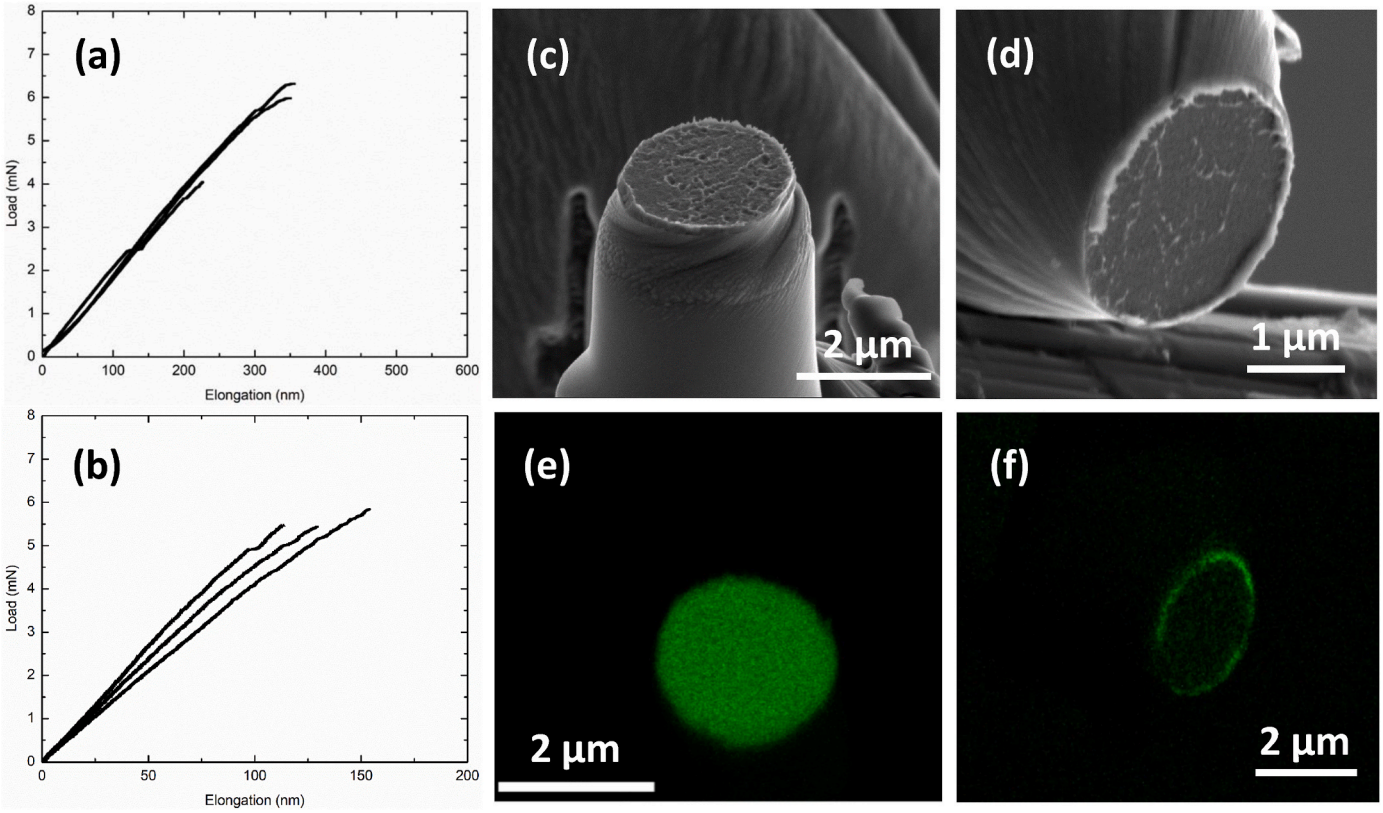

Fig. 7. Tension testing results of TiN/Cu/TiN sandwich micro-pillar specimens: **(a)** load-displacement curves with Cu layer thickness $H = 110$ nm; **(b)** load-displacement curves with $H = 70$ nm; **(c/d)** SE images of the bottom and top portions of the same pillar after tensile separation; **(e/f)** Cu K EDS maps of the bottom and top portions of the same pillar after tensile separation.

was observed at $H = 70$ nm. The findings shown in Fig. 7 illustrate the essential observation that tensile fracture of TiN/Cu/TiN sandwich specimens when H decreases to 110 nm and 70 nm occurred close to or at the TiN/Cu interface. The extensive necking within the Cu layer, observed at $H = 400$ nm, is decidedly absent at $H = 110$ nm and 70 nm.

Several questions arise from the experimental findings regarding tensile failure of epitaxial TiN/Cu/TiN sandwich structures, summarized in Figs. 2–7. The tensile fracture mode exhibits a transition from an extremely ductile fracture within the Cu layer to a relatively brittle fracture close to or at the TiN/Cu interface as the Cu layer thickness decreases from 400 nm to 110 nm and 70 nm. Noting that the structure of the Cu layer remained the same with Cu[110]//TiN[001], the only experimental variable in the tension test is the thickness of the Cu layer H or the ratio of the Cu layer thickness to the diameter of the pillar specimen, H/D. The observed fracture mode transition as H/D varies deserves a mechanistic interpretation. Measured values of the tensile fracture stress, σ_f, appear to saturate at ~1.5 GPa, about one order of magnitude below values of ideal interfacial tensile separation obtained from DFT calculations [45]. This discrepancy suggests that DFT calculations of ideal interfacial separation is missing important physics, what is missing should be clarified. In what follows, results of the accompanying MD simulations shed light on these questions.

3.2. Simulations of Cu nanopillars

Fig. 8 illustrates the global true stress – true strain response of NTDP and NTRP under tensile straining, obtained from the MD simulations of Cu pillars subjected to tensile deformation at a constant strain rate. Strikingly different stress-strain responses are obtained for the NTDP (Fig. 8(a)) and NTRP (Fig. 8(b)). Specifically, the straining response of the disk-shaped Cu nanopillar, Fig. 8(a), is characterized by a maximum flow (or yield) stress which is about 1.5 times larger than the one observed when straining the rod-shaped Cu nanopillar, Fig. 8(b). Moreover, by comparing Fig. 8(a) and (b), one can observe the development of the in-plane stress components, σ_{xx} and σ_{yy}, of significant magnitude within the NTDP. This mechanical response of NTDP to

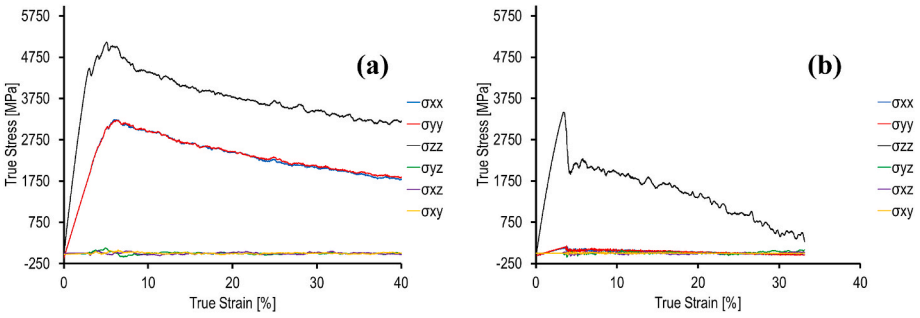

Fig. 8. Global true stress - true strain response from MD simulations for **(a)** NTDP; and **(b)** NTRP.

straining is indeed similar to that found in one of our previous studies using CPFEA simulations [20], in which the magnitude of the hydrostatic stress during tensile loading increased with decreasing thickness of a Cu interlayer between two mechanically rigid loading platens. Both the present MD simulations and the previous CPFEA simulations reveal that the pillar's height to diameter ratio (H/D) plays a critical role in the development of hydrostatic tension within the Cu layer, even though they may not reproduce exactly the experimentally measured load-displacement or stress-strain curves. The effect of H/D on the overall deformation mechanism of Cu nanopillars confined between mechanically rigid substrates during tensile loading at constant strain rate will be discussed below.

The von Mises local shear invariant of the strain tensor was computed in OVITO to obtain additional insights into the dislocation slip activity in Cu nanopillars. Shear strain per atom proves to be a useful property when assessing the pillar shear deformations along arbitrary directions. The final configurations of the deformed nanopillars (both disk-shaped and rod-shaped) with the calculated shear strain per atom are illustrated in Fig. 9. As can be seen from Fig. 9(a), the disk-shaped Cu nanopillar undergoes large shearing deformation. In fact, to accommodate the induced tensile strain, almost the entire pillar structure undergoes plastic deformation. On the other hand, the rod-shaped Cu nanopillar, shown in Fig. 9(b), undergoes a more localized deformation mode characterized by the formation of a neck in which most of the deformation occurs, while significant portions of the pillar, especially those close to the top and bottom walls of NTRP, remain relatively intact. The morphology of the deformed NTRP depicted in Fig. 9(b) resembles qualitatively those observed experimentally for the fractured Cu micropillars shown in Fig. 6(b/c) and 6(d/e). Noting that the top and bottom walls in the MD simulation systems represent the Cu/TiN interface, these results support the existence of a coupling effect between plasticity within the Cu pillar and the presence of the Cu/TiN interfaces where dislocations cannot penetrate from the metal side to the ceramic side. This plays a significant role in the disk-shaped pillar with a small H/D ratio.

Comparison of Fig. 9(a) and (b) reveals that, in the disk-shaped Cu pillar, regions close to the top and bottom walls sustained large plastic deformations, indicating the presence of significant slip activities close to the walls. However, in the rod-shaped Cu pillar, regions close to the walls do not show significant plastic deformation. Based on the growth direction of nano-twinned Cu with [110] parallel to the growth direction Z, the {111}<110> slip systems, with the slip planes oriented 54.7° away from the [110]//Z direction, must have been activated. Therefore, at $H/D < \cot(54.7^\circ) = 0.71$, dislocations gliding on one such slip plane will largely be channeled toward the top and bottom walls without exiting the free sidewall surface, and pile up at the walls due to their impenetrable nature. This is indeed the case for the disk-shaped pillar with $H/D = 0.1613$. The occurrence of heavily plastically deformed regions close to the walls, as observed in Fig. 9(a), can be rationalized through the numerous dislocation slip blockage events, among others. For the rod-shaped pillar shown in Fig. 9(b) with an H/D value of 1.47, dislocations moving on many of the activated slip systems can reach the free sidewall surfaces of the pillar without interference from the top and bottom walls. We state that this is an important reason why regions close to the top and bottom walls remained intact during tensile loading in the rod-shaped pillar. That H/D values adopted in the MD simulations do not correspond to those in the experiments notwithstanding, the simulation output links the presence/absence of significant dislocation activity and dislocation pileup at the wall, or the Cu/TiN interface, to whether brittle fracture will occur there.

4. Discussion

Noell et al. [46] found in their experiments that nanoscale voids form homogeneously within the necked gauge region of a heavily deformed polycrystalline Cu specimen during quasistatic loading at room-temperature. They argued that the homogenous nucleation of nanoscale voids could be best explained by vacancy condensation originating from vacancy supersaturations during a severe plastic deformation process and the presence of hydrostatic tensile stress or stress triaxiality in the specimen neck region.

Voronoi tessellation of the final configuration of the NTDP after 76% straining was used to obtain the local atomic volume. Fig. 10 shows the atomic volume map that was obtained from a 2 nm thick slab region located just below the top wall of the NTDP system. The analysis of the spatial distribution of the atomic volume across the entire slab region reveals the presence of numerous nanovoids. The presence of voids and their location is directly related to that of the large clusters of atoms, colored in red in Fig. 10, in which the atomic volume is significantly

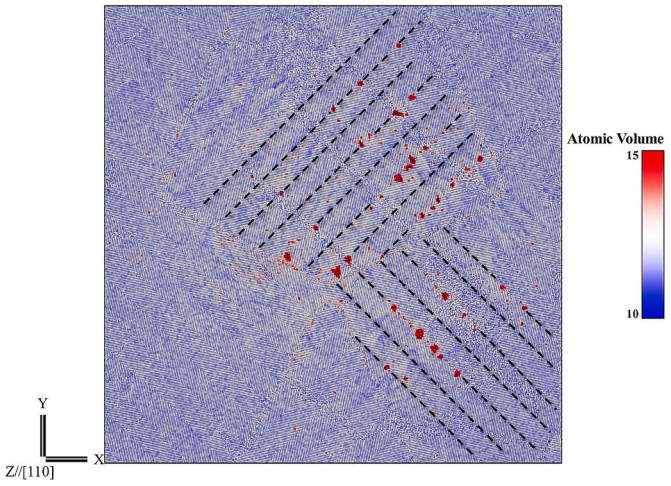

Fig. 10. Estimated volume per atom by performing the Voronoi tessellation over the final configuration of NTDP at 76% strain magnitude in MD simulations. TBs have been marked by the dashed black lines.

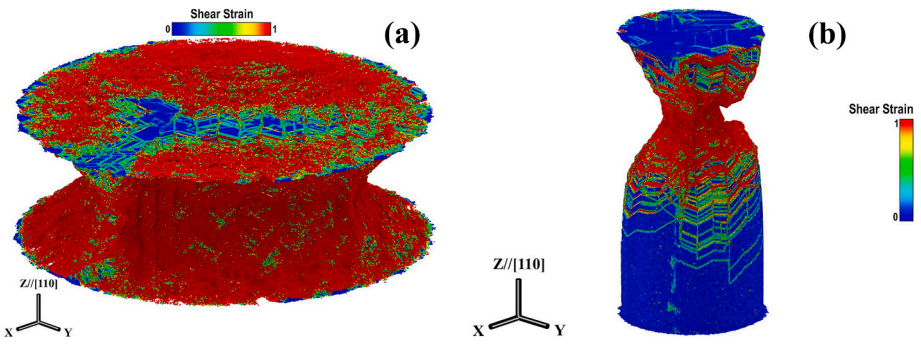

Fig. 9. Calculated von Mises local shear invariant of the strain tensor per atom in MD simulations for **(a)** NTDP and **(b)** NTRP.

larger (up to 50%) than the atomic volume in a perfect crystal structure. Detailed analysis reveals that these nanovoids have a depth of about 1–2 nm in the Z direction. Moreover, Fig. 10 shows that nanovoid formation is more prevalent near twin boundaries, positions of which have been marked by the dashed black lines. The specifics of the dislocation mechanism and the analysis pertaining to the formation of these nanovoids will be presented elsewhere. We emphasize that the formation of nanovoids in our low temperature (T = 300K) MD simulations is indeed consistent with the observations by Noell et al. [44]. In fact, the existence of a high hydrostatic tension in the NTDP under tensile loading, as shown in Fig. 8(a), in combination with the occurrence of significant plastic deformation close to the top and bottom walls as well as the blockage of slip activity by the walls, as illustrated in Fig. 9(a), are the leading contributors to the nucleation and growth of these nanovoids.

According to Noell et al. [44], the tensile fracture in Cu is dominated by the rate of void growth rather than the rate of void nucleation. In other words, a few of the uniformly distributed nanovoids would suffice to cause the ductile fracture after growing into micro-voids. In addition, their study showed that the dislocation structures could be responsible for nanoscale void growth. In fact, as revealed by MD simulations in [47], dislocation processes, e.g., glide and cross-slip, can participate in an adsorption-mediated growth mechanism of a nanoscale void, whose growth rate is dependent on the hydrostatic stress exponentially.

Since combined effects of a notable hydrostatic tension and significant dislocation activities in the regions close to the top and bottom walls of NTDP, shown respectively in Figs. 8(a) and 9(a), caused formation of the nanovoids in Fig. 10, it is reasonable to assume that regions close to the walls of NTDP are prone to fracture under tensile loading. We extend these findings from the MD simulations in analogy to the actual nano-twinned Cu micropillars in the present experiments, shown in Fig. 7. Specifically, the nano-twinned Cu pillars in Fig. 7, with $D > 2$ μm, are characterized by very small H/D values, ≤ 0.07. As argued above, such pillars are capable of channeling dislocations to and blocking them at the Cu/TiN interfaces at much higher rates as compared to pillars with higher H/D, shown in Fig. 6. Thereupon, nanovoids such as those shown in Fig. 10 can form near the Cu/TiN interface, and tensile fracture can be triggered due to growth of just some of these nanovoids. The nanovoid formation can be driven by absorbing the abundant pile-up dislocations close to or at the metal/ceramic interfaces of the micropillar specimens. Driven by the hydrostatic tension, these nanovoids evolve rapidly to microvoids and cause rapid tensile fracture close to or at the Cu/TiN interface, as shown in Fig. 7. This rapid interfacial tensile fracture in turn serves to halt the extensive plastic deformation within the bulk of the Cu layer, leading to an apparent brittle interfacial fracture, in contrast to the pillars with higher H/D shown in Fig. 6.

The present MD simulations link the apparent tensile failure mode of the Cu pillars to dislocation activities, as it is the interaction and pile-up of dislocations that generate either plasticity localization within the Cu bulk or nanovoids close to or at the Cu/TiN interface. This in turn depends on the pillar height-to-diameter ratio. In DFT simulations of ideal tensile separation of metal/ceramic interfaces, dislocation activities and their interaction with the interface, which is impenetrable to dislocations, are not considered. Missing the consideration of dislocation activities and their interaction with the interface, as well as the role of dislocation activity in assisting the nucleation of vacancies and vacancy clusters when they are blocked by the interface, leads to the excessively high tensile separation stress values as calculated by DFT. In addition, it is noted that the presently observed dependence of the apparent tensile failure mode on the aspect ratio of the TiN/Cu/TiN pillars implies that the ductile tensile failure observed within the Cu layer with a thickness of 400 nm may revert back to a more “brittle-like” interfacial failure if the diameter of the tension loaded pillar increases beyond the present 2–3 μm. Extension of this aspect ratio argument to ceramic/metal/ceramic specimens of macroscopic lateral dimensions is interesting, and deserves further investigation.

5. Summary

A combined experimentation/MD simulation study was conducted to probe and understand tensile failure of micro-pillar specimens fabricated from epitaxial TiN/Cu/TiN thin film sandwich structures. The orientation relationship between Cu and TiN is Cu[110]//TiN[001] in the growth direction, and Cu<111>//TiN<100> and Cu<112>//TiN<100> within the growth plane. The Cu layer contains numerous nanotwins with the {111} twin plane parallel to the growth direction, with 2–10 nm wide twin bands rotated in-plane by 90° in different yet symmetry equivalent epitaxial domains. Tensile loading in-situ an SEM measured tensile fracture stress values of ~1.5 GPa and revealed a surprising failure mode transition. At the Cu layer thickness of 400 nm, tensile loading led to ductile fracture occurring within the Cu layer without causing failure of the Cu/TiN interface. As the Cu layer thickness decreases to 110 nm and 70 nm, tensile loading led to brittle fracture occurring close to or at the Cu/TiN interface with little apparent plastic deformation of the Cu layer.

The accompanying MD simulations studied the mechanical response of and defect evolution within Cu nanopillars with different height-to-diameter ratios, confined between rigid walls and placed under tensile loading. A significant hydrostatic stress component develops at small H/D within disk-shaped Cu pillars and is absent within rod-shaped Cu pillars at large H/D. Calculation of the von Mises local shear invariant of the strain tensor further contrasts the mechanical response of disk-shaped and rod-shaped Cu pillars under tensile loading. Cu pillars with large H/D developed localization of dislocation activity, showing necking within the pillar middle portion in qualitative agreement with experimental observations at a Cu layer thickness of 400 nm. In contrast, Cu pillars with small H/D exhibit plasticity throughout the pillar, in particular near the top and bottom rigid walls of the simulation volume which mimic the Cu/TiN interface, impenetrable by dislocations. The high degree of dislocation activities close to or at the top and bottom walls, combined with dislocation pile-up at the rigid wall, serves to create nanovoids close to or at the wall. Under a high hydrostatic tension developed in pillars with small H/D, growth of such nanovoids leads to rapid tensile fracture. While MD simulation of a material volume in exact correspondence with the experimental configuration is prohibitively expensive, the present simulation results offer a good analogy to the experimental situation and mechanistic understanding of tensile failure mechanisms for ceramic/metal/ceramic interfacial regions.

CRediT authorship contribution statement

Xiaoman Zhang: Methodology, Data Collection and Curation, Formal analysis, Investigation, Writing – original draft, Visualization. **Reza Namakian:** Methodology, Software, Data curation, Formal analysis, Investigation, Writing – original draft, Visualization. **Andrew C. Meng:** Methodology, Data Collection and Curation, Formal analysis, Investigation. **Dorel Moldovan:** Conceptualization, Data curation, Validation, Investigation, Resources, Writing – original draft, Writing – review & editing, Supervision, Project administration, Funding acquisition. **W.J. Meng:** Conceptualization, Data Collection and Curation, Validation, Investigation, Resources, Writing – original draft, Writing – review & editing, Supervision, Project administration, Funding acquisition.

Declaration of competing interest

The authors declare that they have no known competing financial interests or personal relationships that could have appeared to influence the work reported in this paper.

Data availability

Data will be made available on request.

Acknowledgments

This work was funded in part by the NSF EPSCoR program, under awards OIA-1541079 and OIA-1946231. Use of experimental facilities at the LSU Shared Instrumentation Facility (SIF), a part of the Louisiana Core User Facilities (CUF), is acknowledged. The simulation portion of this research was conducted with high-performance computational resources provided by Louisiana State University (http://www.hpc.lsu.edu) and the Louisiana Optical Network Infrastructure (http://www.loni.org).

References

[1] H.F. Wang, W.W. Gerberich, J.E. Angelo, Interfacial reactions and adhesion strength of metal/ceramic composites, J. Mater. Res. 10 (9) (1995) 2367–2373.
[2] M. Lane, R.H. Dauskardt, N. Krishna, I. Hashim, Adhesion and reliability of copper interconnects with Ta and TaN barrier layers, J. Mater. Res. 15 (2000) 203–211.
[3] N. Verma, V. Jayaram, Detailed investigation of contact deformation in ZrN/Zr multiplayer—understanding the role of volume fraction, bilayer spacing, and morphology of interfaces, J. Mater. Res. 28 (2013) 3146–3156.
[4] S. Genty, J.-B. Sauvage, P. Tingaut, M. Aufray, Experimental and statistical study of three adherence tests for an epoxy-amine/aluminum alloy system: pull-Off, Single Lap Joint and Three-Point Bending tests, Int. J. Adhesion Adhes. 79 (2017) 50–58.
[5] A. Kubit, T. Katrnak, T. Pytlowany, Influence of the type of adhesive on the properties of the GFRP composite adhesive joint, determined on the basis of the static T-peel test, Adv. Mater. Sci. 21 (2021) 53–74.
[6] ASTM International, Single-Lap-Joint Adhesively Bonded Metal Specimens by Tension Loading (Metal-To-Metal), 2005. ASTM D1002-05: Standard Test Method for Apparent Shear Strength of.
[7] ASTM International, Loading of Single-Lap-Joint Laminated Assemblies, 2007. ASTM D3165-07: Standard Test Method for Strength Properties of Adhesives in Shear by Tension.
[8] ASTM International, ASTM D2095, Standard Test Method for Tensile Strength of Adhesives by Means of Bar and Rod, 2002.
[9] ASTM International, ASTM D897, Standard Test Method for Tensile Properties of Adhesive Bonds, 2012.
[10] ASTM International, T-Peel Test), 2001. ASTM D1876-01: Standard Test Method for Peel Resistance of Adhesives.
[11] L.F.M. da Silva, R.D. Adams, Measurement of the mechanical properties of structural adhesives in tension and shear over a wide range of temperatures, J. Adhes. Sci. Technol. 19 (2005) 109–141.
[12] K. Bobzin, High-performance coatings for cutting tools, CIRP J. Manufact. Sci. Technol. 18 (2017) 1–9.
[13] J.C. Jiang, W.J. Meng, A.G. Evans, C.V. Cooper, Structure and mechanics of W-DLC coated spur gears, Surf. Coat. Technol. 176 (2003) 50–56.
[14] K.C. Mutyala, H. Singh, R.D. Evans, G.L. Doll, Effect of deposition method on the RCF performance of Cr_xN thin film ball coatings, Surf. Coat. Technol. 305 (2016) 176–183.
[15] Adhesion measurements of films and coatings, in: K.L. Mittal (Ed.), Proceedings of the International Symposium on Adhesion Measurement of Films and Coatings 1992, VSP, Utrecht, The Netherlands, 1995.
[16] K.L. Mittal (Ed.), Adhesion Measurements of Films and Coatings, Proceedings of the Second International Symposium on Adhesion Measurement of Films and Coatings 1999, vol. 2, VSP, Utrecht, The Netherlands, 2001.
[17] N.A. Badaluddin, W.F.H.W. Zamri, M.F.M. Din, I.F. Mohamed, J.A. Ghani, Coatings of cutting tools and their contribution to improve mechanical properties: a brief review, Int. J. Appl. Eng. Res. 13 (2018) 11653–11664.
[18] H. Ehsani, J.D. Boyd, J. Wang, M.E. Grady, Evolution of the laser-induced spallation technique in film adhesion measurement, Appl. Mech. Rev. 73 (2021), 030802/1-20.
[19] C.A. Volkert, A.M. Minor, Focused ion beam microscopy and micromachining, MRS Bull. 32 (2007) 389–395.
[20] M.D. Uchic, P.A. Shade, D.M. Dimiduk, Plasticity of micrometer-scale single crystals in compression, Annu. Rev. Mater. Res. 39 (2009) 361–386.
[21] X. Zhang, Y. Mu, M. Dodaran, S. Shao, D. Moldovan, W.J. Meng, Mechanical failure of CrN/Cu/CrN interfacial regions under tensile loading, Acta Mater. 160 (2018) 1–13.
[22] L.E. Toth, Transition Metal Carbides and Nitrides, Academic Press, New York and London, 1971.
[23] B.W. Karr, I. Petrov, P. Desjardins, D.G. Cahill, J.E. Greene, In situ scanning tunneling microscopy studies of the evolution of surface morphology and microstructure in epitaxial TiN(001) grown by ultra-high-vacuum reactive magnetron sputtering, Surf. Coat. Technol. 94–95 (1997) 403–408.
[24] W.J. Meng, G.L. Eesley, Growth and mechanical anisotropy of TiN thin films, Thin Solid Films 271 (1995) 108–116.
[25] W.C. Chen, S.T. Wu, Epitaxial growth of TiN on Al2O3 at cryogenic temperature, Japn. J. Appl. Phys. Part 2 - Letters & Express Letters 42 (2003) L192–L193.
[26] X. Zhang, S. Shao, A.S.M. Miraz, C.D. Wick, B.R. Ramachandran, W.J. Meng, Low temperature growth of Cu thin films on TiN(001) templates: structure and energetics, Materialia 12 (2020) 100748/1–10074813.
[27] R. Namakian, B.R. Novak, X. Zhang, W.J. Meng, D. Moldovan, A combined molecular dynamics/Monte Carlo simulation of Cu thin film growth on TiN substrates: illustration of growth mechanisms and comparison with experiments, Appl. Surf. Sci. 570 (2021) 151013/1–15101320.
[28] J.R. Smith, T. Hong, D.J. Srolovitz, Metal-ceramic adhesion and the Harris functional, Phys. Rev. Lett. 72 (1994) 4021–4024.
[29] D.J. Siegel, L.G. Hector, J.B. Adams, Ab initio study of Al-ceramic interfacial adhesion, Phys. Rev. B 67 (2003), 092105/1-4.
[30] K.M. Carling, E.A. Carter, Effects of segregating elements on the adhesive strength and structure of the α-Al2O3/β-NiAl interface, Acta Mater. 55 (2007) 2791–2803.
[31] T. Hong, J.R. Smith, D.J. Srolovitz, Impurity effects on adhesion: Nb, C, O, B, and S at a Mo/$MoSi_2$ interface, Phys. Rev. B 47 (1993) 13615–13625.
[32] T. Hong, J.R. Smith, D.J. Srolovitz, Theory of metal-ceramic adhesion, Acta Metall. Mater. 43 (1995) 2721–2730.
[33] S. Plimpton, Fast parallel algorithms for short-range molecular dynamics, J. Comput. Phys. 117 (1995) 1–19.
[34] Y. Mishin, M.J. Mehl, D.A. Papaconstantopoulos, A.F. Voter, J.D. Kress, Structural stability and lattice defects in copper:Ab initio, tight-binding, and embedded-atom calculations, Phys. Rev. B 63 (22) (2001), 224106.
[35] W.S. Ko, A. Stukowski, R. Hadian, A. Nematollahi, J.B. Jeon, W.S. Choi, G. Dehm, J. Neugebauer, C. Kirchlechner, B. Grabowski, Atomistic deformation behavior of single and twin crystalline Cu nanopillars with preexisting dislocations, Acta Mater. 197 (2020) 54–68.
[36] P. Hirel, Atomsk: a tool for manipulating and converting atomic data files, Comput. Phys. Commun. 197 (2015) 212–219.
[37] P.M. Larsen, Revisiting the Common Neighbour Analysis and the Centrosymmetry Parameter, arXiv:2003.08879v1 [physics>comp-ph].
[38] A. Stukowski, Visualization and analysis of atomistic simulation data with OVITO - the open visualization tool, Model. Simulat. Mater. Sci. Eng. 18 (2010), 015012.
[39] D. Surblys, H. Matsubara, G. Kikugawa, T. Ohara, Application of atomic stress to compute heat flux via molecular dynamics for systems with many-body interactions, Phys. Rev. E 99 (2019), 051301.
[40] D. Surblys, H. Matsubara, G. Kikugawa, T. Ohara, Methodology and meaning of computing heat flux via atomic stress in systems with constraint dynamics, J. Appl. Phys. 130 (2021), 215104.
[41] J. Guenole, W.G. Nohring, A. Vaid, F. Houlle, Z. Xie, A. Prakash, E. Bitzek, Assessment and optimization of the fast inertial relaxation engine (FIRE) for energy minimization in atomistic simulations and its implementation in LAMMPS, Comput. Mater. Sci. 175 (2020), 109584.
[42] G. Bussi, D. Donadio, M. Parrinello, Canonical sampling through velocity rescaling, J. Chem. Phys. 126 (2007), 014101.
[43] A.S.M. Miraz, N. Dhariwal, W.J. Meng, B.R. Ramachandran, C.D. Wick, Development and application of interatomic potentials to study the stability and shear strength of Ti/TiN and Cu/TiN interfaces, Mater. Des. 196 (2020) 109123/1–10912314.
[44] A.M. Hodge, Y.M. Wang, T.W. Barbee, Mechanical deformation of high-purity sputter-deposited nano-twinned copper, Scripta Mater. 59 (2008) 163–166.
[45] A.S.M. Miraz, W.J. Meng, B.R. Ramachandran, C.D. Wick, Computational observation of the strengthening of Cu/TiN metal/ceramic interfaces by sub-nanometer interlayers and dopants, Appl. Surf. Sci. 554 (2021), 149562.
[46] P.J. Noell, J.E.C. Sabisch, D.L. Medlin, B.L. Boyce, Nanoscale conditions for ductile void nucleation in copper: vacancy condensation and the growth-limited microstructural state, Acta Mater. 184 (2020) 211–224.
[47] R.B. Sills, B.L. Boyce, Void growth by dislocation adsorption, Mater. Res. Lett. 8 (2020) 103–109.